Chapter 2

The Migration of Diffuse Photon Density Waves through Highly Scattering Media

When light enters a highly scattering (or turbid) medium such as a cloud, milk, or tissue, the photons do not simply reflect back from or transmit through the medium as they would for a pane of glass. Instead, the individual photons scatter many times and thus trace out random paths before escaping from or being absorbed by the medium.

In this chapter I consider the collective properties of these scattered photons. When the intensity of a point source in a turbid medium with uniform optical properties is sinusoidally modulated, a macroscopic wave of photon density develops, and propagates spherically outwards from the source. Although microscopically the individual photons follow random walk-like trajectories, macroscopically a coherent photon density wave is created.

After experimentally verifying the existence of these waves, I examine their refraction at planar interfaces between media with different optical properties and their refraction and diffraction by objects with different optical properties than the surrounding media. I show that the perturbation of the diffuse photon density wavefronts is captured by standard refraction, diffraction, and scattering models.

The theoretical basis of this work derives from the photon diffusion equation. The radiative transport equation is a more accurate model for the migration of photons in general, but is typically difficult to handle. I start this chapter by reviewing the

assumptions that reduce the general transport equation to a diffusion equation. The classical wave behavior of DPDW's is then considered. At the end of the chapter, the breakdown of the diffusion approximation is considered as well as higher order approximations to the transport equation.

2.1 Diffusion Approximation to the Transport Equation

The linear transport equation for photons propagating in media that scatters and absorbs photons is [54, 55, 56]

$$\frac{1}{v}\frac{\partial L(\mathbf{r},\hat{\Omega},t)}{\partial t} + \nabla \cdot L(\mathbf{r},\hat{\Omega},t)\hat{\Omega} + \mu_t L(\mathbf{r},\hat{\Omega},t) = \mu_s \int L(\mathbf{r},\hat{\Omega}',t) f(\hat{\Omega},\hat{\Omega}') \mathrm{d}\hat{\Omega}' + S(\mathbf{r},\hat{\Omega},t) \; . \tag{2.1}$$

$L(\mathbf{r},\hat{\Omega},t)$ is the radiance at position $\mathbf{r}$, traveling in direction $\hat{\Omega}$, at time t, with units of W m^{-2} sr^{-1} (sr = steradian = unit solid angle). The normalized phase function $f(\hat{\Omega},\hat{\Omega}')$ represents the probability of scattering into a direction $\hat{\Omega}'$ from direction $\hat{\Omega}$. v is the speed of light in the medium and $\mu_t = \mu_s + \mu_a$ is the transport coefficient where μ_s is the scattering coefficient and μ_a is the absorption coefficient. $S(\mathbf{r},\hat{\Omega},t)$ is the spatial and angular distribution of the source with units of W m^{-3} sr^{-1}. The photon fluence is given by

$$\Phi(\mathbf{r},t) = \int \mathrm{d}\hat{\Omega} L(\mathbf{r},\hat{\Omega},t) \; . \tag{2.2}$$

The photon flux, or current density, is given by

$$\mathbf{J}(\mathbf{r},t) = \int \mathrm{d}\hat{\Omega} L(\mathbf{r},\hat{\Omega},t)\hat{\Omega} \; . \tag{2.3}$$

Both the fluence and the flux have units of W m^{-2}. The linear transport equation neglects coherence and polarization effects. Recently, however, Ackerson *et al.* have successfully included coherence effects within a transport model [57, 58]. Photon polarization within the transport equation has also been considered by Fernandez and Molinari [59].

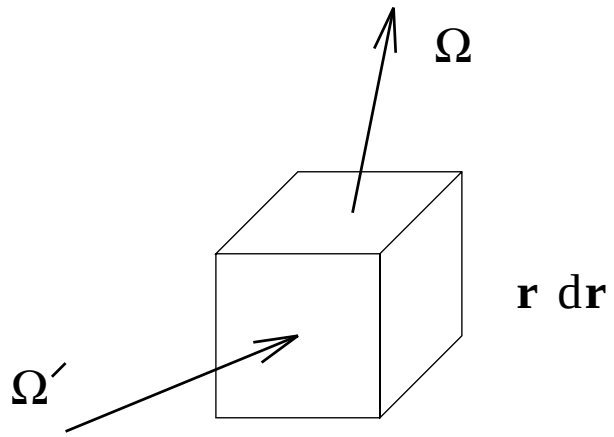

Figure 2.1: A schematic of the conservation of photons in a small element in phase space. The phase element is at position $\mathbf{r}$, time t, and direction $\hat{\Omega}$. Photons scattered from all directions $\hat{\Omega}'$ into direction $\hat{\Omega}$ at position $\mathbf{r}$ must be considered. Also, the scattering from direction $\hat{\Omega}$ and absorption within the phase element must be considered as well as the flux of photons through the phase element.

The transport equation can be thought of as a conservation equation for the radiance. If we consider a small element in phase space, that is a small volume around position $\mathbf{r}$ and a small solid angle around $\hat{\Omega}$ at time t (see fig. 2.1), the left-hand side of eq. (2.1) accounts for photons leaving the small element, and the right-hand side accounts for photons entering the small element. The first term on the left-hand side is the time-derivative of the radiance which equals the number of photons entering the element minus the number leaving. The second term accounts for the flux of photons along the direction $\hat{\Omega}$. The third term accounts for the scattering and absorption of photons within the phase element. Photons scattered from an element in phase space are balanced by the scattering into another element in phase space. The balance is handled by the integral on the right-hand side of eq. (2.1) which accounts for photons at position $\mathbf{r}$ being scattered from all directions $\hat{\Omega}'$ into direction $\hat{\Omega}$. The second term on the right-hand side is the source of photons.

Analytic solutions of the transport equation are difficult to obtain and numerical calculations require large amounts of computational power. Solutions typically exist only for simple geometries such as planar geometries with plane wave illumination

[60], some spherical geometries [61], and a few other special cases [62].

These difficulties are reduced by considering approximate solutions to the transport equation. A standard approximation method for the transport equation is known as the P_N approximation [54, 55, 56]. The method of the P_N approximation is simply to expand the radiance, phase function, and source in spherical harmonics $Y_{l,m}$, truncating the series for the radiance at $l = N$. The radiance and source are expanded as

$$L(\mathbf{r}, \hat{\Omega}, t) = \sum_{l=0}^{N} \sum_{m=-l}^{l} \phi_{l,m}(\mathbf{r}, t) Y_{l,m}(\hat{\Omega}) \ , \tag{2.4}$$

and

$$S(\mathbf{r}, \hat{\Omega}, t) = \sum_{l=0}^{N} \sum_{m=-l}^{l} q_{l,m}(\mathbf{r}, t) Y_{l,m}(\hat{\Omega}) \ . \tag{2.5}$$

By substituting eq. (2.4) into eq. (2.2) we see that $\phi_{0,0}$ is proportional to the photon fluence. By substituting eq. (2.4) into eq. (2.3) we see that $\phi_{1,m}$ are the components of the photon flux. The $q_{l,m}(\mathbf{r}, t)$ are the amplitudes of the different angular moments of the source at position $\mathbf{r}$ and time t.

For the phase function, we make the reasonable assumption that the scattering amplitude is only dependent on the change in direction of the photon, and thus

$$\begin{aligned} f(\hat{\Omega} \cdot \hat{\Omega}') &= \sum_{l=0}^{\infty} \frac{2l+1}{4\pi} g_l P_l(\hat{\Omega} \cdot \hat{\Omega}') \\ &= \sum_{l=0}^{\infty} \sum_{m=-l}^{l} g_l Y^*_{l,m}(\hat{\Omega}') Y_{l,m}(\hat{\Omega}) \ , \end{aligned} \tag{2.6}$$

where P_l is a Legendre Polynomial of order l and the second line is obtained using the standard angular addition rule [63]. The phase function is normalized so that $g_0 = 1$. Note that g_1 is the average cosine of the scattering angle.

The P_1 approximation is quite good when the albedo $c = \mu_s/(\mu_s + \mu_a)$ is close to unity, the phase function is not too anisotropic (e.g. $g_1 < .99$, but this depends on the optical properties), and the source-detector separation is large compared to $1/(\mu_s(1 - g_1))$. Within the P_1 approximation the radiance can be written as

$$L(\mathbf{r}, \hat{\Omega}, t) = \frac{1}{4\pi} \Phi(\mathbf{r}, t) + \frac{3}{4\pi} \mathbf{J}(\mathbf{r}, t) \cdot \hat{\Omega} \ . \tag{2.7}$$

Similarly the photon source can be written as

$$S(\mathbf{r},\hat{\Omega},t) = \frac{1}{4\pi}S_0(\mathbf{r},t) + \frac{3}{4\pi}\mathbf{S_1}(\mathbf{r},t)\cdot\hat{\Omega}\ , \tag{2.8}$$

where $S_0(\mathbf{r},t)$ and $\mathbf{S_1}(\mathbf{r},t)$ are respectively the monopole (isotropic) and dipole moments of the source.

Inserting eq. (2.7) and eq. (2.8) into eq. (2.1) and integrating over $\hat{\Omega}$ yields

$$\frac{1}{v}\frac{\partial}{\partial t}\Phi(\mathbf{r},t) + \mu_a\Phi(\mathbf{r},t) + \nabla\cdot\mathbf{J}(\mathbf{r},t) = S_0(\mathbf{r},t)\ . \tag{2.9}$$

Inserting eq. (2.7) and eq. (2.8) into eq. (2.1), multiplying by $\hat{\Omega}$, and integrating over $\hat{\Omega}$ yields

$$\frac{1}{v}\frac{\partial}{\partial t}\mathbf{J}(\mathbf{r},t) + (\mu_s' + \mu_a)\mathbf{J}(\mathbf{r},t) + \frac{1}{3}\nabla\Phi(\mathbf{r},t) = \mathbf{S_1}(\mathbf{r},t)\ , \tag{2.10}$$

where $\mu_s' = \mu_s(1-g_1)$ is the reduced scattering coefficient.

We obtain the P_1 equation by decoupling eq. (2.9) and eq. (2.10) for $\Phi(\mathbf{r},t)$,

$$\begin{aligned} -D\nabla^2\Phi(\mathbf{r},t) + v\mu_a\Phi(\mathbf{r},t) + \frac{\partial\Phi(\mathbf{r},t)}{\partial t} + \underline{\frac{3D}{v}\left[\mu_a\frac{\partial\Phi(\mathbf{r},t)}{\partial t} + \frac{1}{v}\frac{\partial^2\Phi(\mathbf{r},t)}{\partial t^2}\right]} \\ = vS_0(\mathbf{r},t) + \underline{\frac{3D}{v}\frac{\partial S_0}{\partial t} - 3D\nabla\cdot\mathbf{S_1}(\mathbf{r},t)}\ . \end{aligned} \tag{2.11}$$

$D = v/(3\mu_s')$ is the photon diffusion coefficient. The absorption coefficient is dropped from the photon diffusion coefficient to keep the set of approximations consistent. That is, the P_1 approximation is valid when the albedo is close to unity and the scattering is not highly anisotropic and thus $\mu_a \ll \mu_s'$. This has been discussed in greater detail by Furutsu and Yamada [64]. The scattering coefficient and scattering anisotropy do not explicitly appear in the P_1 equation (and subsequently the diffusion equation) but instead appear together as the reduced scattering coefficient. This interplay between the scattering coefficient and anisotropy to produce an "effective" scattering coefficient is known as the similarity relation [65, 66, 67].

The standard photon diffusion equation is obtained when the underlined terms in eq. (2.11) are dropped. Dropping the dipole moment of the source is justified by assuming an isotropic source. This assumption is usually supported by treating

collimated sources as isotropic sources displaced one transport mean free path into the scattering medium from the collimated source. The assumption for dropping the other terms is best seen in the frequency-domain where the time dependence of the source is taken as $\exp(-i\omega t)$. When the intensity of the source is sinusoidally modulated then the photon fluence becomes $\Phi(\mathbf{r})\exp(-i\omega t)$. The time derivatives can then be replaced by $-i\omega$ and the rest of the underlined terms can be ignored when $3D\omega/v^2 \ll 1$. This assumption is equivalent to $v\mu_s'/\omega \gg 1$, that is the scattering frequency must be much larger than the modulation frequency.

Given these assumptions we arrive at the photon diffusion equation for $\Phi(\mathbf{r},t)$,

$$-D\nabla^2\Phi(\mathbf{r},t) + v\mu_a\Phi(\mathbf{r},t) + \frac{\partial\Phi(\mathbf{r},t)}{\partial t} = vS_0(\mathbf{r},t) \ . \tag{2.12}$$

Note that in the frequency-domain the photon diffusion equation can be rewritten as the Helmholtz equation

$$(\nabla^2 + k_{AC}^2)\Phi_{AC}(\mathbf{r}) = \frac{-v}{D}S_0(\mathbf{r}) \ , \tag{2.13}$$

where the wavenumber is complex, i.e.

$$k_{AC}^2 = \frac{-v\mu_a + i\omega}{D} \ . \tag{2.14}$$

2.2 Diffuse Photon Density Waves

When the source of photons in a turbid medium is intensity modulated, e.g. $S(\mathbf{r},t) = S_{DC}(\mathbf{r}) + S_{AC}(\mathbf{r})\exp(-i\omega t)$, then the photon fluence will oscillate at the same frequency. This small but measurable traveling wave disturbance of the light energy density is referred to as a diffuse photon density wave [3, 21, 22, 23, 68].

Diffuse photon density waves are scalar, damped, traveling waves. These traveling waves arise formally in any diffusive system that is driven by an oscillating source such as in heat conduction [69] and chemical waves [70]. Fishkin and Gratton for example [21], have calculated the light energy density, U(r,t), within an optically dense homogenous media in the presence of a modulated point light source at the

origin. They then used the result and the principle of superposition to derive the light energy density in the presence of an absorbing semi-infinite plane. The oscillatory part of the solution for an infinite, homogenous dense random media with an intensity modulated point source is [21, 68]

$$\Phi_{AC}(\mathbf{r},t) = \frac{vS_{AC}}{4\pi Dr}\exp(ikr)\exp(-i\omega t)\ . \tag{2.15}$$

S_{AC} is the source modulation amplitude, $D = v/(3\mu_s')$ is the photon diffusion coefficient in the turbid medium where v is the speed of light in the medium and μ_s' is the reduced scattering coefficient, ω is the angular modulation frequency, and the wavenumber k is given by

$$\begin{aligned} k &= \sqrt{\frac{-v\mu_a + i\omega}{D}} \\ &= (-1)^{1/2}\left(\frac{v^2\mu_a^2+\omega^2}{D^2}\right)^{1/4}\exp\left(-\frac{i}{2}\tan^{-1}\frac{\omega}{v\mu_a}\right) \\ &= \left(\frac{v^2\mu_a^2+\omega^2}{D^2}\right)^{1/4}\left[i\cos\left(\frac{1}{2}\tan^{-1}\frac{\omega}{v\mu_a}\right)+\sin\left(\frac{1}{2}\tan^{-1}\frac{\omega}{v\mu_a}\right)\right]\ . \end{aligned} \tag{2.16}$$

This is not the only solution for k, however it is the solution which satisfies the physical condition that the amplitude is exponentially attenuated rather than growing (i.e. the imaginary part of k is greater than zero). This particular solution is obtained by extracting the -1 from the rest of the equation on the second line. An analogous equation for k can be found using the following approach (still requiring the imaginary part of k to be greater than zero):

$$\begin{aligned} k &= x + iy\ , \\ k^2 &= (x^2-y^2) + i2xy\ , \\ x^2-y^2 &= \frac{-v\mu_a}{D}\ , \\ 2xy &= \frac{\omega}{D}\ , \\ k &= \sqrt{\frac{v\mu_a}{2D}}\left[\left(\sqrt{1+\left(\frac{\omega}{v\mu_a}\right)^2}+1\right)^{1/2} + i\left(\sqrt{1+\left(\frac{\omega}{v\mu_a}\right)^2}-1\right)^{1/2}\right] \end{aligned} \tag{2.17}$$

Note that the solution for an intensity modulated point source, eq. (2.15), is a spherical wave with a complex wavenumber. The complex wavenumber indicates that the wave is exponentially attenuated and has a well defined wavelength, amplitude, and phase at all points. Qualitatively this wavelength corresponds to the root-mean-square displacement experienced by a typical photon during a single modulation period. It can be altered by modifying D, μ_a, or ω. This wave does not, on average, transport any energy. The net diffusive energy transport arises in the DC (i.e. non-oscillating) part of the process.

To experimentally verify the existence of diffuse photon density waves, we used the experimental system described in section 6.1 to generate and measure a modulated photon fluence. The measurements were made in a tank containing a highly scattering emulsion known as Intralipid [71, 72, 73, 74]. Measurements of the phase and amplitude of the diffuse photon density wave (DPDW) were measured with respect to the source at each point on a 0.5 cm square grid. The dimensions of the grid were small compared with the dimensions of the tank so that the medium is a good approximation of an infinite medium.

The results for an Intralipid concentration of 0.5% are exhibited in fig. 2.2. Constant phase countours are shown at 20 degree intervals about the source. Notice that the contours are circular, and that their radii can be extrapolated back to the source. The phase shift and the quantity $\ln|r\Phi_{AC}(\mathbf{r})|$ are plotted as a function of radial distance from the source in the inset of fig. 2.2. The relationships are linear as expected and give us the real and imaginary parts of the diffuse photon density wavenumber. From these measurements we deduce the wavelength of the diffuse photon density wave (11.2 cm). The equations for the real and imaginary parts of the wavenumber can be solved for the reduced scattering coefficient and absorption coefficient of the medium, i.e.

$$\mu_a = \frac{\omega}{v}\left[\tan\left(2\tan^{-1}\frac{k_r}{k_i}\right)\right]^{-1}, \tag{2.18}$$

$$\mu_s' = \frac{k_r^2 + k_i^2}{3\left(\mu_a^2 + \frac{\omega^2}{v^2}\right)^{1/2}} . \tag{2.19}$$

Here k_r and k_i are respectively the real and imaginary parts of the wavenumber. Using eq. (2.18) and eq. (2.19) we find that μ_s'=5.0 cm^{-1} and μ_a=0.019 cm^{-1} for 0.5% Intralipid at 22°C. The photon absorption can be attributed almost entirely to water [75].

2.3 Interaction with Free-Space Boundaries

Diffuse photon density waves propagating in infinite homogeneous media are spherical waves. If the turbid medium is not infinite or homogeneous, then the wave fronts are distorted. Here I consider homogeneous media that have a boundary between the turbid media and media which do not scatter light. Microscopically, the perturbation of the diffuse photon density wave arises from photons escaping into the non-scattering medium. When a photon crosses the boundary from the turbid medium into the non-scattering medium, there is no mechanism for changing the direction of the photon to return it to the turbid medium except for Fresnel reflections at the boundary. This photon escape reduces the number of photons in the wave front, thus reducing the amplitude and altering the phase. Generally the long path length photons are more likely to escape, reducing the mean path length and the DPDW wavelength. Thus the phase tends to increase because of the presence of a free-space boundary.

Within the diffusion approximation, the exact boundary condition for an index matched free-space boundary is that the component of the flux normal to the interface, pointing from the non-scattering medium into the turbid medium, must be zero. Specifically, [76, 77]

$$J_{in}(\mathbf{r}) = \frac{1}{4}\Phi(\mathbf{r}) + \frac{D}{2v}\hat{n}\cdot\nabla\Phi(\mathbf{r}) = 0 , \tag{2.20}$$

where $\hat{n}$ is the normal to the boundary pointing away from the turbid medium and $\mathbf{r}$ is on the boundary. This boundary condition is known as the zero partial flux boundary

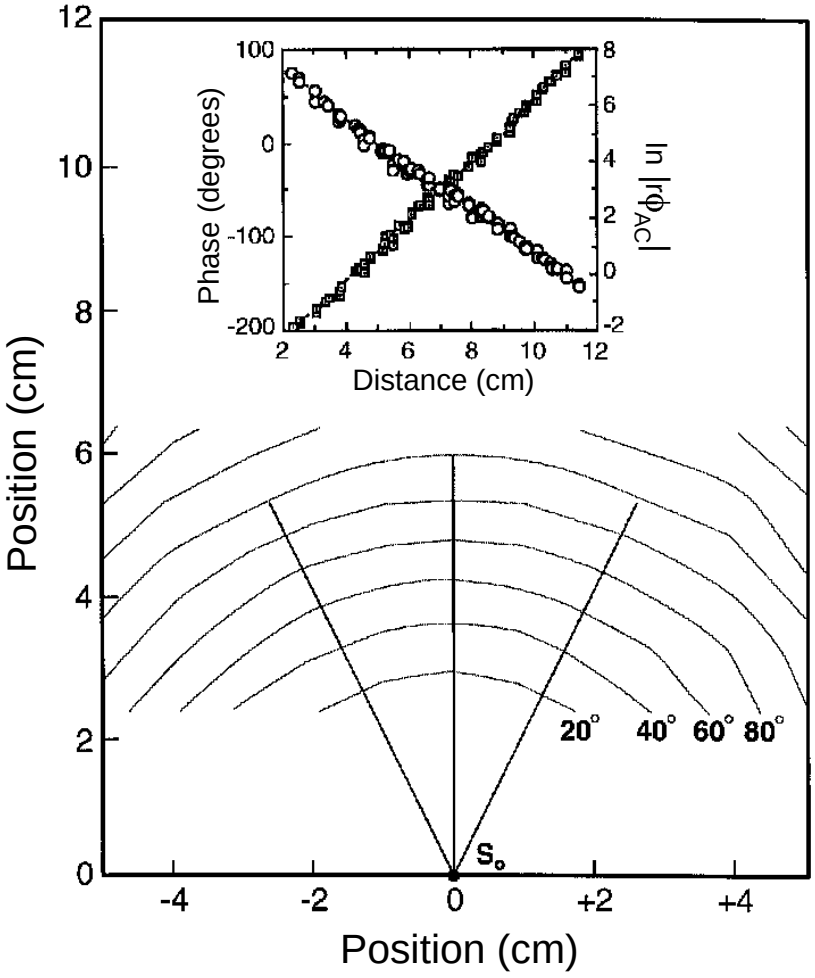

Figure 2.2: Constant phase contours shown as a function of position for a homogeneous, 0.5% solution of Intralipid. The contours are shown in 20 degree intervals. Inset: The measured phase shift (circles), and $\ln|r\Phi_{AC}(\mathbf{r})|$ (squares) are plotted as a function of radial distance from the source So.

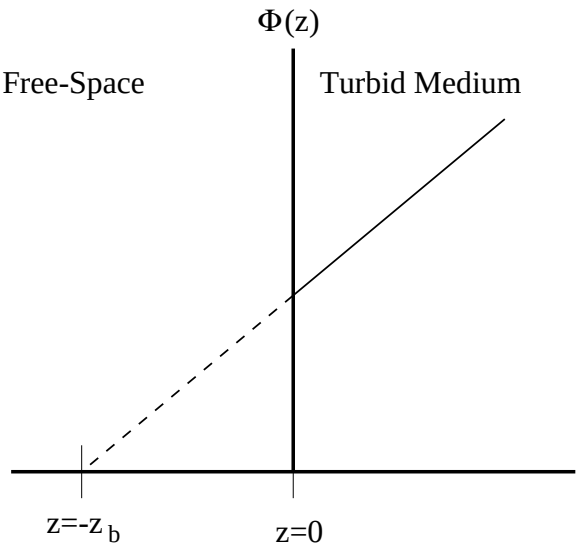

Figure 2.3: Schematic of the extrapolated zero boundary condition.

condition. At the boundary, we measure the outward component of the flux

$$\begin{aligned} J_{out}(\mathbf{r}) &= \frac{1}{4}\Phi(\mathbf{r}) - \frac{D}{2v}\hat{n}\cdot\nabla\Phi(\mathbf{r}) \\ &= \frac{1}{2}\Phi(\mathbf{r}) = -\frac{D}{v}\hat{n}\cdot\nabla\Phi(\mathbf{r}) \ . \end{aligned} \tag{2.21}$$

The second line is derived from the condition that $J_{in} = 0$ on the boundary and shows that what we measure on the boundary is proportional to the fluence and the component of the flux normal to the boundary.

Generally it is difficult to obtain analytic solutions of the diffusion equation using the zero partial flux boundary condition. Instead the approximate extrapolated zero boundary condition is used. This requires the fluence to be zero at a distance of $2/(3\mu_s')$ from the actual boundary. For example, for a semi-infinite medium with the boundary at $z = 0$ and the turbid medium at $z > 0$ the extrapolated zero boundary condition requires $\Phi(z_b) = 0$, where $z_b = -2/(3\mu_s')$. This extrapolation distance comes from a linear extrapolation of the fluence at the boundary to the zero crossing point (see fig. 2.3). It is argued that $z_b = -0.7104/\mu_s'$ gives better agreement with the photon transport equation [78, 79]. Here I use $z_b = -2/(3\mu_s')$ to remain consistent with the recent literature (e.g [76]).

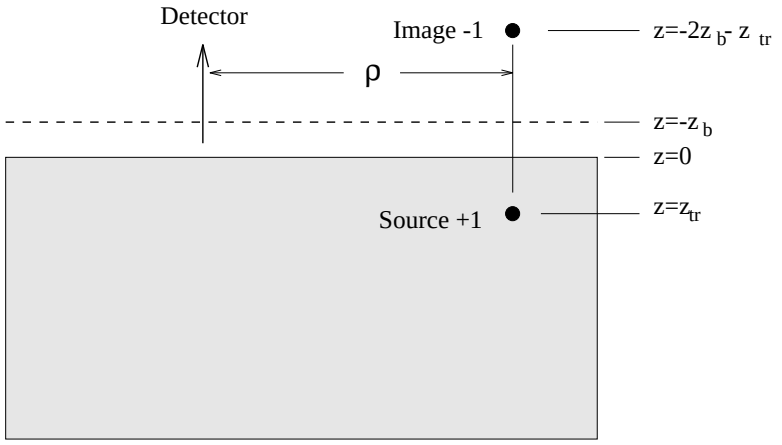

Figure 2.4: Schematic of source and image source positions for a semi-infinite medium.

For a semi-infinite medium, the solution of the diffusion equation (with the extrapolated zero boundary condition) is easily obtained by using image sources. That is an image of the real source is formed by reflection of the real source about the plane of the extrapolated zero boundary (see fig. 2.4). Note that collimated sources are usually approximated as isotropic point sources which are displaced a distance $z_{tr} = l^* = 1/\mu_s'$ from the collimated source. Given the source and image source configuration shown in fig. 2.4, the solution of the diffusion equation for a semi-infinite medium with a collimated source on the real boundary is

$$\Phi(\rho_d, z_d) = \frac{vS \exp\left(ik\sqrt{\rho_d^2 + (z_d - z_{tr})^2}\right)}{4\pi D\sqrt{\rho_d^2 + (z_d - z_{tr})^2}} - \frac{vS \exp\left(ik\sqrt{\rho_d^2 + (z_d + z_{tr} + 2z_b)^2}\right)}{4\pi D\sqrt{\rho_d^2 + (z_d + z_{tr} + 2z_b)^2}}. \tag{2.22}$$

The source is at $\rho = 0$ and $z = 0$ while the detector is at $\rho = \rho_d$ and $z = z_d$. A useful form of eq. (2.22) is when the detector is on the real boundary ($z_d = 0$) and $\rho \gg z_{tr}$. Under these conditions eq. (2.22) reduces to

$$\Phi(\rho_d, 0) = \frac{vS \exp(ik\rho)}{4\pi D\rho^2}\left[-4ik\left(z_b^2 + z_b z_{tr}\right)\right] . \tag{2.23}$$

If there is a mismatch in the indices of refraction between the turbid medium and free-space then the exact boundary condition is not the zero partial flux boundary condition because photons are being reflected at the interface back into the turbid

medium. In this case the exact boundary condition is [76, 77]

$$J_{in}(\mathbf{r}) = \frac{1}{4}\Phi(\mathbf{r}) + \frac{D}{2v}\hat{n}\cdot\nabla\Phi(\mathbf{r}) = R_\phi\frac{1}{4}\Phi(\mathbf{r}) - R_j\frac{D}{2v}\hat{n}\cdot\nabla\Phi(\mathbf{r}) \ , \tag{2.24}$$

where R_ϕ and R_j are respectively the reflection coefficient for the isotropic fluence and the reflection coefficient for the anisotropic flux. They are given by [76]

$$R_\phi = \int_0^{\pi/2} 2\sin\theta\cos\theta R_{\text{Fresnel}}(\theta)\mathrm{d}\theta \ , \tag{2.25}$$

$$R_j = \int_0^{\pi/2} 3\sin\theta\cos^2\theta R_{\text{Fresnel}}(\theta)\mathrm{d}\theta \ , \tag{2.26}$$

where $R_{\text{Fresnel}}(\theta)$ is the Fresnel reflection coefficient for unpolarized light [76]

$$\begin{aligned} R_{\text{Fresnel}}(\theta) &= \frac{1}{2}\left(\frac{n_{in}\cos\theta' - n_{out}\cos\theta}{n_{in}\cos\theta' + n_{out}\cos\theta}\right)^2 \\ &+ \frac{1}{2}\left(\frac{n_{in}\cos\theta - n_{out}\cos\theta'}{n_{in}\cos\theta + n_{out}\cos\theta'}\right)^2 \quad \text{when } 0 \le \theta \le \theta_c \ , \\ &= 1 \qquad\qquad\qquad\qquad\qquad\qquad \text{when } \theta_c \le \theta \le \pi/2 \ . \end{aligned} \tag{2.27}$$

The angle of incidence, θ, is given with respect to the boundary normal, the refracted angle, θ', is given by $n_{in}\sin\theta = n_{out}\sin\theta'$, and n_{in} and n_{out} are respectively the index of refraction inside and outside the turbid medium. This condition is called the partial flux boundary condition. The partial flux boundary condition can be reduced to an extrapolated zero boundary condition where

$$z_b = \frac{1 + R_{eff}}{1 - R_{eff}}\frac{2}{3}l^* \ , \tag{2.28}$$

where

$$R_{eff} = \frac{R_\phi + R_j}{2 - R_\phi + R_j} \ . \tag{2.29}$$

This boundary condition is described in detail by Haskell *et al.* [76] and Aronson [77].

2.4 Refraction and Diffraction of Diffuse Photon Density Waves

In this section I present experiments which illustrate the refraction and diffraction of diffuse photon density waves. I demonstrate that the refraction of these waves at

planar interfaces is well described by Snell's Law [22]. In addition, I demonstrate that simple diffractive and refractive models can be used to understand the scattering of these waves by absorptive and dispersive objects embedded in an otherwise uniform system [28].

2.4.1 Refraction at planar interfaces

Fig. 2.5 demonstrates the refraction of these waves in three ways. A planar boundary has been introduced, separating the lower medium, with Intralipid concentration c_l=1.0% and light diffusion coefficient D_l, from the upper medium, with Intralipid concentration c_u= 0.25% and light diffusion coefficient D_u. In fig. 2.5 contours of constant phase are drawn every 20° for the propagation of the DPDW from the lower medium to the upper medium. The contours below the boundary are the homogenous media contours (without reflection); they are obtained before the partition is introduced into the sample. The contours above the boundary are derived from the diffuse photon density waves transmitted into the less concentrated medium. As a result of the detector geometry, the closest approach to the partition is about 1 cm.

We expect a number of general results. First, the wavelength in the less dense medium (λ_u = 14.8 cm) should be greater than the wavelength of the diffuse photon density wave in the incident medium (λ_l = 8.17 cm). This was observed. The ratio of the two wavelengths should equal the ratio of the diffusional indices of refraction of the two media. Specifically we see, as expected, that $\lambda_u = \lambda_l\sqrt{D_l/D_u} = \lambda_l\sqrt{c_l/c_u}$ (this relation holds when absorption is negligible). Furthermore, we would expect that the apparent source position (S_i), as viewed from within the upper medium, should be shifted from the real source position (S_o = 4.0 ± 0.2 cm) by a factor λ_l/λ_u = 0.55 as predicted by Snell's law for paraxial waves. This is what we find within the accuracy of this measurement. Using the radii from the full contour plots we see that the apparent source position is shifted from 4.0 ± 0.2 cm to 2.0 ± 0.25 cm from the planar interface.

Finally, fig. 2.5 explicitly demonstrates Snell's law for diffuse photon density

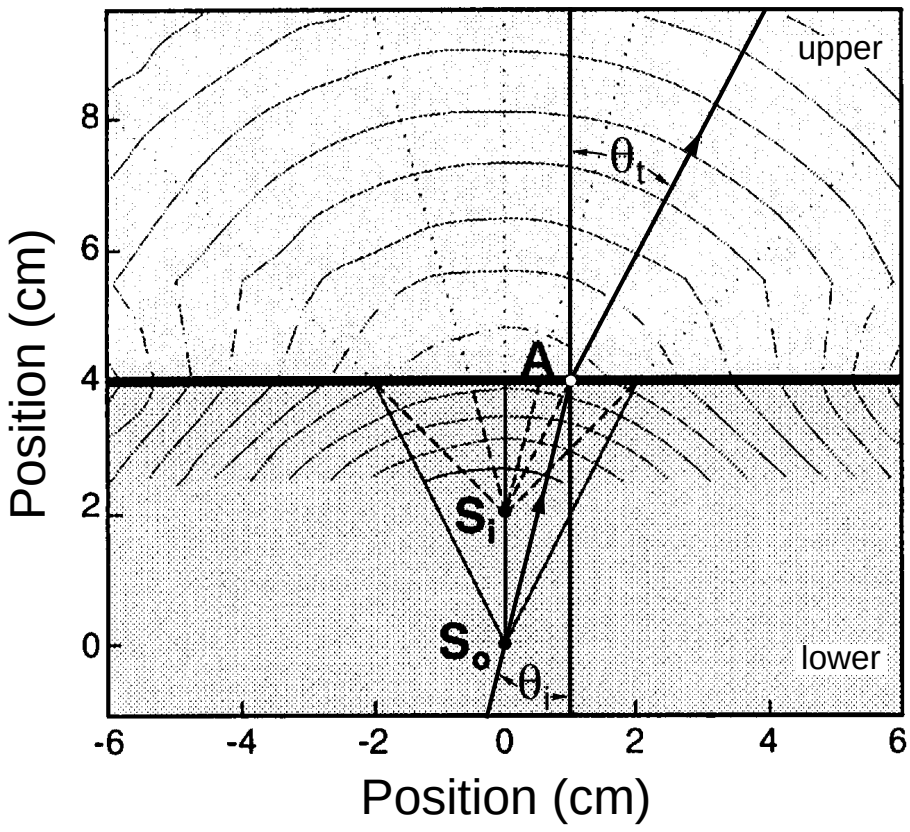

Figure 2.5: Constant phase contours (in 20 degree intervals) as a function of position showing the propagation of a diffuse photon density wave across a planar boundary that separates 1% concentrated Intralipid from 0.25% Intralipid. S_o, source position; S_i, apparent source position ; A, point on boundary; θ_i, angle of incident ray; θ_t, angle of refracted ray. The solid lines are obtained directly from data. The dot-dashed lines are obtained by interpolation over large distances, and are drawn to show the irregularities at large angles.

waves. This can be seen by following the ray from S_o to the point A at the boundary, and then into the upper medium. The ray in the lower medium makes an angle $\theta_i = 14°$ with respect to the surface normal. The upper ray is constructed in the standard way between the apparent source position S_i, through the point A on the boundary, and into the medium above the boundary [80]. It is perpendicular to the circular wavefronts in the less dense medium and makes an angle $\theta_t = 26.6°$ with respect to the boundary normal. Within the accuracy of the experiment, we see that $\sin\theta_i / \sin\theta_t = 0.54 \approx \lambda_l/\lambda_u$, so that Snell's law accurately describes the propagation of diffuse photon density waves across the boundary. The wavefronts become quite distorted when the source ray angle exceeds ~ 30 degrees. These irregularities are a consequence of total internal reflection, diffraction, and spurious boundary effects.

2.4.2 Refraction and diffraction by spherical inhomogeneities

Here I present measurements of diffuse photon density wavefront distortions that arise when these waves are perturbed by purely absorptive or dispersive homogeneous spheres. In general one would expect both refractive and diffractive processes to affect the wavefronts. Unfortunately, our intuition from conventional optics is of limited applicability, since we must work in the near field. Measurements of wavefront distortions from purely absorbing spheres are reasonably well described by a simple diffraction model whereby the diffuse photon density wave is scattered by an absorbing disk of the same diameter. The pure dispersive case is qualitatively different. Here a ray optic model works well for scatterers characterized by a larger light diffusion coefficient relative to that of the surrounding turbid medium, but a diffractive model is required under the opposite conditions.

The diffraction of DPDW's by absorptive spheres is illustrated in fig. 2.6. The contours of constant phase and amplitude are plotted for a DPDW traveling in different concentrations of Intralipid and diffracting around a 4.0 cm diameter absorptive sphere. The sphere was saturated with ink so that the fraction of incident light transmitted through the sphere was below the detection limit of $\sim 10^{-6}$. Nevertheless, the

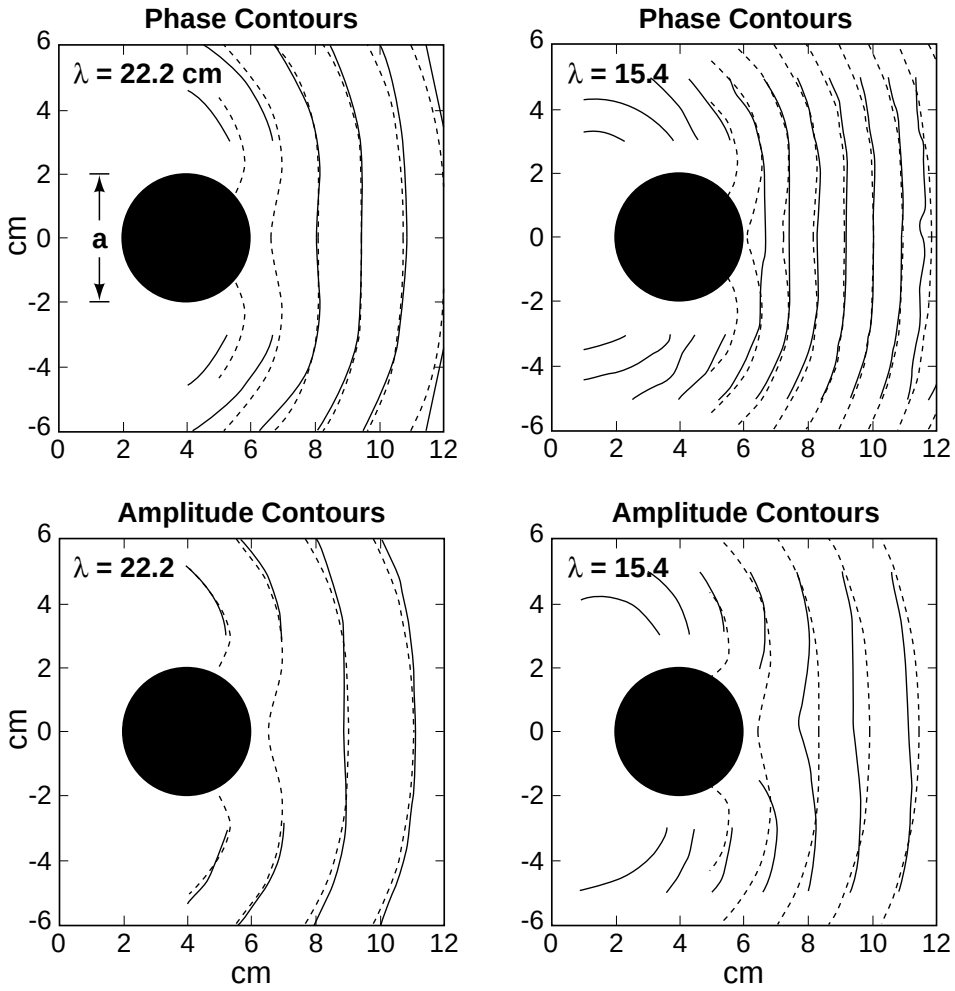

Figure 2.6: The diffraction of a diffuse photon density wave by a spherical absorber with a diameter of 4.0 cm. The light source is at the origin and generates a wave with a wavelength of 22.2 cm in the plots on the left, and a wavelength of 15.4 cm in the plots on the right. Our experimental (theoretical) results are the solid (dashed) curves. The phase contours are plotted every 20 degrees and the amplitude contours are plotted in decreasing intervals of e^{-1}.

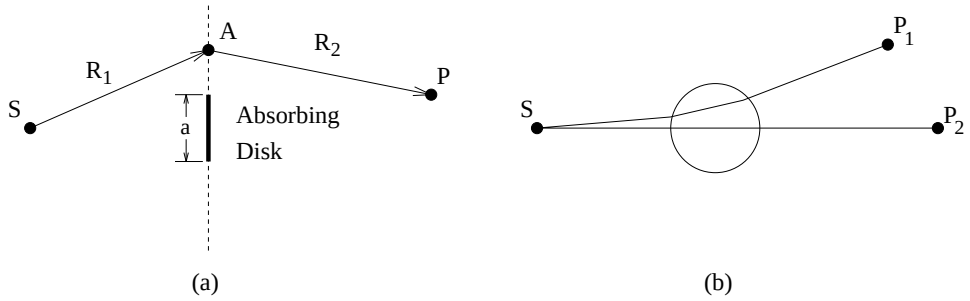

Figure 2.7: (a) In the diffraction model the sphere is replaced by an absorbing disk of the same diameter (a=4.0 cm) which lies in a plane through the center of the sphere. R_1 is the distance from the source, S, to a point A in the diffraction plane (dashed line) and R_2 is the distance from A to the image point, P. Here we take the z-axis to be normal to the diffraction plane, and we let the diffraction plane coincide with the xy-plane (i.e. z=0). The wavefront at P is calculated by integrating the standard Kirchoff equation over the diffraction plane. (b) In the ray model the wavefront is calculated by determining the phase and amplitude of rays which are refracted through a spherical lens.

wavefronts on the other side of the sphere are detected. These wavefronts are formed by the diffraction of the wave around the sphere.

Here, I have modeled this effect in a simple way. In the model, I replaced the sphere by a totally absorbing disk of the same diameter. The disk was chosen to lie in a plane containing the center of the sphere, with surface normal pointing in the z direction. The diffraction from this disk can be calculated using the standard Kirchoff construction [81]

$$\Phi(x_p, y_p = 0, z_p) = \frac{kz_p}{2\pi i} \int_S \mathrm{d}x \; \mathrm{d}y \; \Phi(R_1) \frac{\exp(ikR_2)}{R_2^2} \left[\frac{i}{kR_2} + 1 \right] \; . \tag{2.30}$$

The construction is depicted in fig. 2.7a. Here $\Phi(R_1)$ is the complex amplitude of the photon fluence in the plane of the disk, R_1 is the length of the vector from the source at position $R_s = (x_s = 0, y_s = 0, z_s)$ to a point $A = (x, y, z = 0)$ on the diffraction plane, R_2 is the length of the vector going from A to the detection point $R_p = (x_p, y_p = 0, z_p)$. The Green's function is derived from the point source solution for diffuse photon density waves in an infinite homogeneous medium so that k is complex. Specifically, the Green's function for this problem is derived from

a superposition of Green's function solutions of the Helmholtz equation. I chose a superposition to satisfy Dirichlet boundary conditions on the diffraction plane at z=0. Therefore, eq. (2.30) is derived from the integral of $\Phi(R_1)\frac{\partial G_D(R_2,R_2')}{\partial z}\mathrm{d}x\mathrm{d}y$ over the diffraction plane, with $G_D(R_2,R_2') = \left[\exp(ikR_2)/R_2 - \exp(ikR_2')/R_2'\right]/4\pi$, where $\mathbf{R_2} = \mathbf{R_p} - \mathbf{A}$, $\mathbf{R_2'} = \mathbf{R_p'} - \mathbf{A}$, and $\mathbf{R_p'}$ is just the image of $\mathbf{R_p}$ reflected about the diffraction plane.

The experimental (theoretical) results are the solid (dotted) curves in fig. 2.6. The simple model approximates the measured wavefront distortion reasonably well. Note that there are no free parameters in the fit. The model appears to fit the experimental results better for bigger ratios of diffuse photon density wavelength to object diameter. Of course, the function $\Phi(R_1)$ in the plane of the disk is only approximately correct as a result of shadowing and diffraction by the front portion of the sphere. A similar effect will modify the scattered wave. This effect is expected to be larger as the wavelength decreases as observed in fig. 2.6. Nevertheless the model captures the qualitative physics of the scattering.

The constant phase contours (solid line) arising from the scattering of a non-absorptive sphere are shown in fig. 2.8. The Intralipid surrounding the sphere had the same concentration in both experiments, but the concentration of Intralipid inside the sphere was either lesser (fig. 2.8a) or greater (fig. 2.8b) than the surrounding medium. The observed patterns are different. These effects can be approximated using a ray optics model in the first case and a diffraction model in the second case.

In the ray optic model the scatterer is treated like a spherical lens with a different diffusional index of refraction than the surrounding medium. The basic idea of the model is depicted in fig. 2.7b. The complex wave amplitude is calculated from the amplitude and phase for points along the rays emerging from the source. Some of the rays were refracted through the sphere, others were not. This model ignores multiple scattering in the sphere since the waves are heavily damped.

Again, we do not expect the model to give perfect quantitative agreement with the measurements since diffraction effects are omitted. However, when the rays trans-

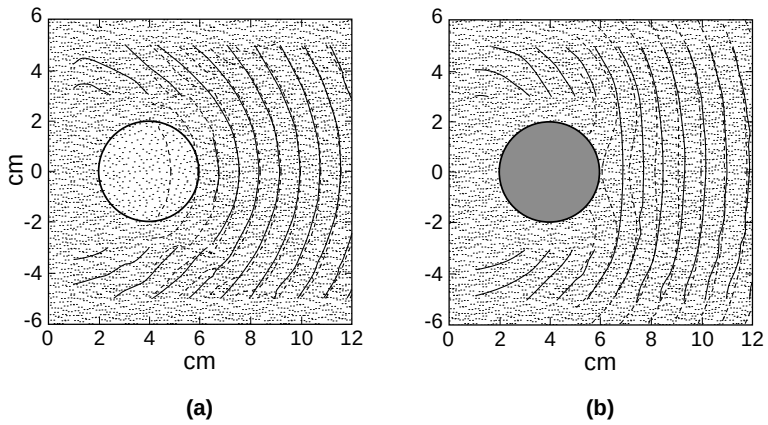

Figure 2.8: The scattering of a diffuse photon density waves by purely dispersive spheres. (a) The Intralipid concentration within the spherical shell is 0.125%, less than the surrounding medium. (b) The Intralipid concentration is 2.8%, greater than the surrounding medium. For both, the surrounding Intralipid is the same, the source is located at the origin, the sphere has a diameter of 4.0 cm, and is centered at x=4.0 cm, y=0.0 cm. The phase contours are drawn every 20 degrees for the experimental (solid lines) and theoretical (dashed lines) results. The theoretical results were calculated in (a) by the ray model and in (b) by the diffraction model.

mitted through the sphere are attenuated less than the rays outside of the sphere, we would expect diffraction effects to be negligible. This is the case when the sphere has a smaller concentration of Intralipid than the surrounding medium, and the expected behavior was observed (see fig. 2.8a). For near axis rays the model also predicts an apparent source position at $z_s = 3.5$ cm. This is easily verified by standard ray construction techniques.

The ray method does not work well for dense spheres. The dense sphere acts more like an absorber, since the diffuse photon density wave is significantly attenuated upon traveling through the sphere. For this reason one might expect the purely diffractive model discussed earlier to work better. Indeed this is what was observed (see fig. 2.8b).

2.5 Scattering of Diffuse Photon Density Waves

The previous section showed that diffuse photon density waves are distorted by the presence of optical inhomogeneities. The degree of distortion is determined by the characteristics of the inhomogeneity such as its position, shape, size, and scattering and absorption properties. We saw that in some cases the perturbation can be modeled using a simple diffraction or ray optic model. A better theory for the observed perturbation is desirable for many reasons. In particular, the simple models discussed in the previous section only work for specific differences in the optical properties and specific source-detector positions relative to the inhomogeneity. That is, the object must be placed between the source and detector, and it must be highly absorbing relative to the background or have a smaller scattering coefficient with no absorption contrast. Since the Helmholtz equation is known to describe the transport of DPDW's in a piecewise homogeneous media [22, 82], we expect that an exact solution exists for the scattering of DPDW's by spherical objects [29, 30, 31]. The solutions will be similar to, and simpler than, the theory of Mie scattering [83] often used in optics.

In this section I derive the analytic solution of the Helmholtz equation for a piecewise homogeneous system consisting of a spherical object composed of one highly scattering medium embedded in a second highly scattering medium of infinite spatial extent. This solution is easily extended to semi-infinite media using the extrapolated zero boundary condition [4, 54, 56, 76]. The analytic solution is compared with experimental data in order to assess the theory's predictive power, and a simple inverse localization algorithm is demonstrated to determine the size and location of a spherical object. Finally, the theory is extended to include more complex problems in imaging.

2.5.1 An Analytic Solution

The derivation of the analytic solution for the scattering of DPDW's from spherical inhomogeneities begins with the Helmholtz equation (eq. (2.13)). In the presence of a spherical heterogeneity, the photon fluence is found by constructing a general solution

to eq. (2.13) outside and inside the sphere and applying the appropriate boundary conditions. It is natural to analyze the problem in spherical coordinates whose origin coincides with the center of the spherical object (see fig. 2.9). The general solution outside the sphere is a superposition of incident and scattered waves [63], i.e.

$$\Phi_{out} = \Phi_{inc} + \Phi_{scatt} \tag{2.31}$$

where

$$\begin{aligned} \Phi_{inc} &= \frac{vS_{AC}}{4\pi D|\mathbf{r}-\mathbf{r_s}|}\exp(ik^{out}|\mathbf{r}-\mathbf{r_s}|) \\ &= i\frac{vS_{AC}k^{out}}{D}\sum_{l=0}^{\infty} j_l(k^{out}r_<)h_l^{(1)}(k^{out}r_>)\sum_{m=-l}^{l} Y_{l,m}^*(\theta_s,\phi_s)Y_{l,m}(\theta,\phi) \end{aligned} \tag{2.32}$$

is the spherical wave created by the source and incident on the sphere.

$$\Phi_{scatt} = \sum_{l,m}\Big[A_{l,m}j_l(k^{out}r) + B_{l,m}n_l(k^{out}r)\Big]Y_{l,m}(\theta,\phi) \tag{2.33}$$

is the wave scattered from the object.

Inside the sphere, the general solution is

$$\Phi_{in} = \sum_{l,m}\Big[C_{l,m}j_l(k^{in}r) + D_{l,m}n_l(k^{in}r)\Big]Y_{l,m}(\theta,\phi)\ . \tag{2.34}$$

Here, $j_l(x)$ and $n_l(x)$ are Spherical Bessel and Neumann functions respectively, $h_l^{(1)}(x)$ are the Hankel functions of the first kind, $Y_{l,m}(\theta,\phi)$ are the spherical harmonics, k^{out} and k^{in} are the complex wavenumbers outside and inside the sphere respectively, $\mathbf{r}$ ($\mathbf{r_s}$) is the position of the detector (source) measured from the center of the sphere, and $r_<$ ($r_>$) is the smaller (larger) of $|\mathbf{r}|$ and $|\mathbf{r_s}|$. The unknown parameters ($A_{l,m}$, $B_{l,m}$, $C_{l,m}$, $D_{l,m}$) are determined using the following boundary conditions: (a) Φ must be finite everywhere except at a source, (b) Φ_{out} must asymptotically approach a spherically outgoing wave as $r \to \infty$, (c) the flux normal to the boundary must be continuous, i.e. $D_{out}\hat{r}\cdot\nabla\Phi_{out} = D_{in}\hat{r}\cdot\nabla\Phi_{in}$ where D_{out} (D_{in}) is the photon diffusion coefficient outside (inside) the sphere, and (d) the photon fluence must be continuous across the boundary, i.e. $\Phi_{in} = \Phi_{out}$ at $r = a$ [56, 82].

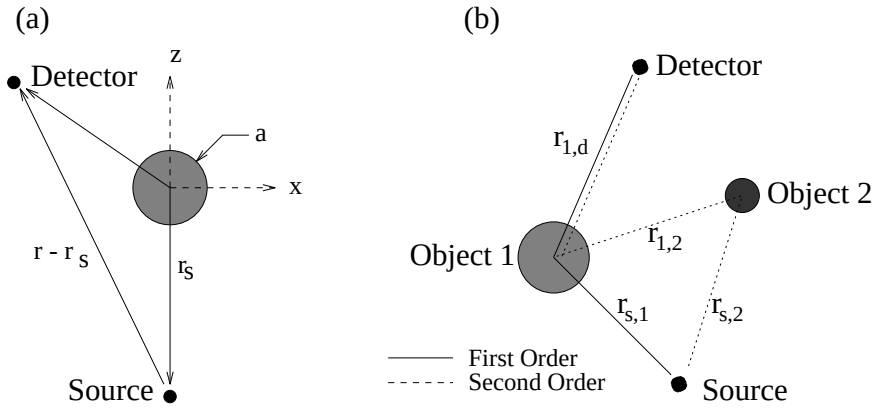

Figure 2.9: To solve the Helmholtz equation for a spherical boundary it is natural to use spherical coordinates with the origin at the center of the object (a). The source is positioned on the z-axis ($\theta_s = \pi$) to exploit the azimuthal symmetry of the problem, and the relevant distances between the source, object, and detector are indicated in the figure. Scattering from multiple objects is diagrammed in (b). The first and second order waves scattered from the first object are illustrated by the solid and dashed line respectively. The relevant distances are indicated in the diagram.

Considering these boundary conditions and using the orthogonality relation for the spherical harmonics [84], I find

$$A_{l,m} = -i\frac{vS_{AC}k^{out}}{D}h_l^{(1)}(k^{out}z_s)Y^*_{l,m}(\pi,0)\left[\frac{D_{out}xj_l'(x)j_l(y) - D_{in}yj_l(x)j_l'(y)}{D_{out}xh_l^{(1)\prime}(x)j_l(y) - D_{in}yh_l^{(1)}(x)j_l'(y)}\right] , \tag{2.35}$$

$$B_{l,m} = iA_{l,m} , \tag{2.36}$$

$$C_{l,m} = -i\frac{vS_{AC}k^{out}}{D}h_l^{(1)}(k^{out}z_s)Y^*_{l,m}(\pi,0)\left[\frac{D_{out}xh_l^{(1)}(x)j_l'(x) - D_{out}xh_l^{(1)\prime}(x)j_l(x)}{D_{out}xh_l^{(1)\prime}(x)j_l(y) - D_{in}yh_l^{(1)}(x)j_l'(y)}\right] , \tag{2.37}$$

$$D_{l,m} = 0 , \tag{2.38}$$

where $x = k^{out}a$, $y = k^{in}a$, $\mathbf{r_s} = (r = z_s, \theta = \pi, \phi = 0)$, and j_l' and $h_l^{(1)\prime}$ are the first derivatives of the functions j_l and $h_l^{(1)}$ with respect to the argument. Placing the source on the z-axis exploits the azimuthal symmetry of the problem leading to $A_{l,m} = C_{l,m} = 0$ for $m \neq 0$. The distortion of the wave is entirely dependent on the parameters $k^{out} = k(\omega, \mu_s'^{out}, \mu_a^{out})$, $k^{in} = k(\omega, \mu_s'^{in}, \mu_a^{in})$, D_{out}, D_{in}, $\mathbf{r_s}$, and the object

radius a. In general the infinite sum for Φ_{out} converges, permitting the sum to be truncated after obtaining the desired precision. The proceeding calculations require no more than 20 terms in the series to obtain better than 10^{-5} precision, which far exceeds experimental precision. On a Sun Microsystems (Mountain View, CA) Sparc 2, Φ_{out} can be calculated 10-100 times per second (depending on the above mentioned parameters).

For the special case wherein the heterogeneity is a perfect absorber, I satisfy the zero partial flux boundary condition

$$\frac{1}{4}\Phi(\mathbf{r}) - \frac{D}{2v}\frac{\partial}{\partial r}\Phi(\mathbf{r}) = 0 \tag{2.39}$$

at $r = a$. Of course $\Phi_{in} = 0$. The solution in this case is

$$A_{l,m} = -i\frac{v S_{AC} k^{out}}{D} h_l^{(1)}(k^{out} z_s) Y_{l,m}^*(\pi, 0) \left[\frac{j_l(x) - \frac{2k^{out}}{3\mu_s'} j_l'(x)}{h_l^{(1)}(x) - \frac{2k^{out}}{3\mu_s'} h_l^{(1)\prime}(x)} \right] \ . \tag{2.40}$$

$$B_{l,m} = iA_{l,m} \ , \tag{2.41}$$

$$C_{l,m} = 0 \ , \tag{2.42}$$

$$D_{l,m} = 0 \ . \tag{2.43}$$

The analytic solutions enable us to estimate the measurement precision required to detect optical inhomogeneities. The required phase precision is determined from the position-dependent difference in phase between the incident wave and the distorted wave, while the required amplitude precision is found from the position-dependent ratio of $|\Phi_{out}|/|\Phi_{inc}|$. Contour plots of the phase difference and the amplitude ratio indicate the spatial positions which are most sensitive to the presence of the object as well as the required signal-to-noise ratio. Fig. 2.10 illustrates this spatially-dependent sensitivity for a perfectly absorbing sphere immersed in a medium with $\mu_s' = 10.0$ cm^{-1} and $\mu_a = 0.02$ cm^{-1}. These plots show that 1.0° phase and 10.0% amplitude precision is sufficent for localization with measurements made in the shadow (within 4.0 cm of the object) of the 1.0 cm diameter absorber. This is well within the 0.1° phase and 0.1% amplitude precision available with current detectors. Localization of smaller

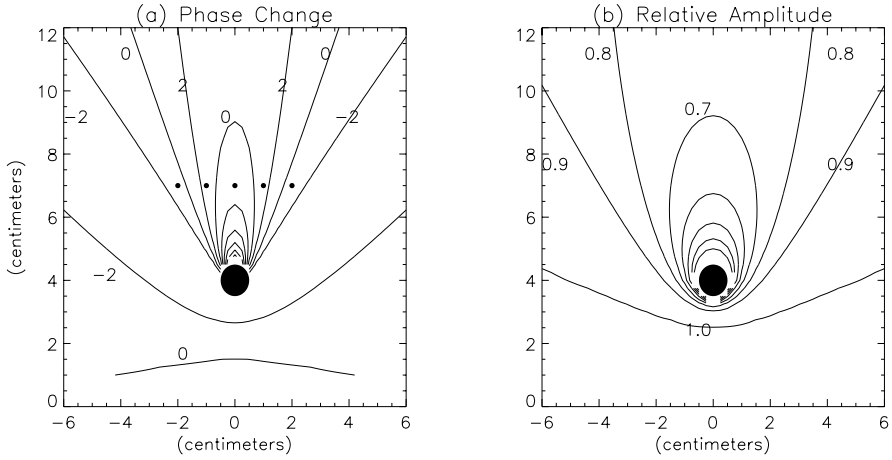

Figure 2.10: These sensitivity plots demonstrate the phase and amplitude resolution necessary to measure a DPDW distorted by a perfect absorber. Plotted in (a) is the phase difference between an incident wave and the wave distorted by a 1.0 cm diameter absorber. The ratio of the amplitude of the distorted wave with respect to the incident wave is plotted in (b). For these plots, the surrounding medium's optical characteristics are μ_s'=10 cm^{-1} and μ_a=0.02 cm^{-1}, the modulation freq. is 200 MHz, and $v = 2.25 \cdot 10^{10}$ cm/s. The dots in (a) represent the locations where measurements were made in order to characterize the object.

absorbers will require better precision. A more detailed signal-to-noise analysis that reveals the limits to detecting, localizing, and characterizing is given in chapter 3.

2.5.2 Experimental Verification of the Analytic Solution

Two sets of experiments were performed, one to check the validity of the theory and the other to resolve object characteristics by fitting the theory to experimental data. In the first set of experiments, the object and source are fixed in the Intralipid with a separation z_s. The phase and amplitude of the distorted DPDW are measured by moving the detector to different points on a two-dimensional grid containing the source and the center of the object. These experimental results are then compared to the prediction of eq. (2.31) for the given object properties. In the second set of experiments, the properties of different spherical absorbers are found by fitting the theory to a measurement of the distorted wavefront along a line. This was accomplished by minimizing the least squares theoretical fit to the experimental data using the object position and radius as free parameters. The optical properties of the Intralipid were determined before each experiment through separate measurements of phase and amplitude of the DPDW propagating in the infinite homogeneous system [3, 21]. These quantities were used in the subsequent analysis.

The measurements indicate that the analytic theory accurately predicts the distortion of the DPDW. Furthermore, because of the close agreement, we are able to characterize a spherical absorber embedded in the turbid medium. These observations were not obvious *a priori* for one major reason: the theory is derived from the diffusion equation, but photon migration is better approximated by a transport equation. In fact, significant differences between the diffusion equation and the transport equation arise near sharp boundaries. As mentioned below, evidence of these differences have been detected.

The measured distortion of the DPDW by a perfectly absorbing sphere is shown in fig. 2.11 and compared to the predicted distortion. This comparison illustrates that the analytic solution shows good agreement with the experimental data.

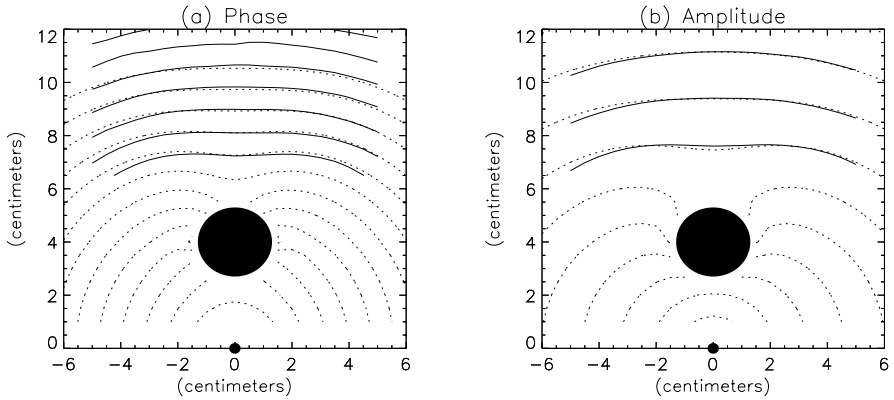

Figure 2.11: The experimental measurements (solid lines) of a DPDW distorted by a 1.3 cm radius perfect absorber are compared to the theoretical prediction (dotted lines) for the given experimental parameters. Phase contours are drawn every 20 degrees in (a), while the amplitude contours are drawn every $e^{-0.5}$. For this experiment, the optical properties of the surrounding medium were μ_s'=3.0 cm^{-1} and μ_a=0.02 cm^{-1}, f =200 MHz, and $v = 2.25 \cdot 10^{10}$ cm/s.

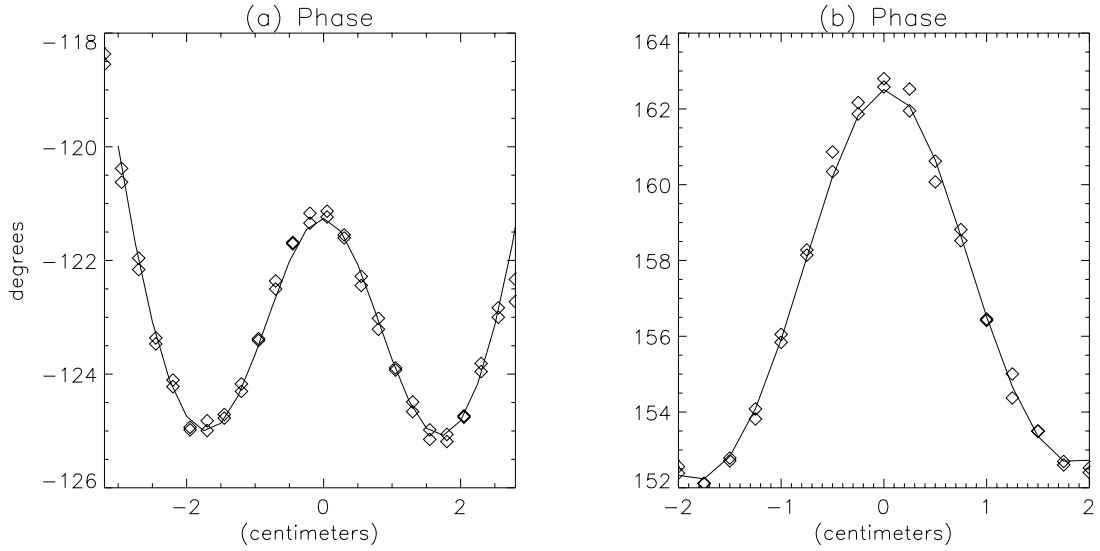

Figure 2.12: The fits to experiment C and G from table 2.1 are presented in (a) and (b) respectively. The experimental data ($\diamond$'s) are compared to the best fit (solid line). The experimental parameters are given in table 2.1.

Table 2.1: The results of fitting theory to a series of experimental observations of a DPDW scattered by an absorber are presented in this table. The absorber had a radius of $a_{exp} = 1.3$ cm and was positioned at $Z = 4.0$ cm, $X = 0.0$ cm, and $Y = 0.0$ cm. For each experiment, the detector was positioned at $Z_{detector}$ and scanned from $-2.0 < X < 2.0$. The experiments were performed in different concentrations of Intralipid for which the photon random walk step is given by l^*. In all experiments, $\mu_a = 0.02$ cm^{-1}, $f = 200$ MHz, and $v = 2.25 \cdot 10^{10}$ cm/s.

Exp.	$Z_{detector}$	Intralipid	$l^* = 1/\mu_s'$	Z_{fit}	X_{fit}	Y_{fit}	a_{fit}
	cm		cm	cm	cm	cm	cm
A	6.5	0.25%	0.60	3.87	-0.05	0.08	1.02
B	7.5	0.25%	0.60	4.08	-0.06	-0.56	1.04
C	6.5	0.50%	0.33	4.06	0.00	-0.13	1.12
D	7.5	0.50%	0.33	4.01	-0.02	0.08	1.15
E	6.5	0.75%	0.23	4.20	0.01	-0.07	1.15
F	7.5	0.75%	0.23	4.11	0.00	0.12	1.20
G	6.5	1.00%	0.18	4.12	0.02	0.00	1.22
H	7.5	1.00%	0.18	4.17	0.00	0.04	1.21

As an example of the utility of the analytic solution, a simple least-squares fitting algorithm was used to fit the analytic solution to the measurements of phase and amplitude of the DPDW to predict object size and location. Measurements were taken along lines parallel to those indicated in fig. 2.10a. The results of these experiments are presented in table 2.1. Fits for two of these experiments are shown in fig. 2.12.

The results in table 2.1 show that a fit to measurements made in the shadow of the object determines the x and y position of the absorber to an accuracy of ± 0.1 cm and the z position to ± 0.2 cm. Finally, the object radius was determined to within ± 0.3

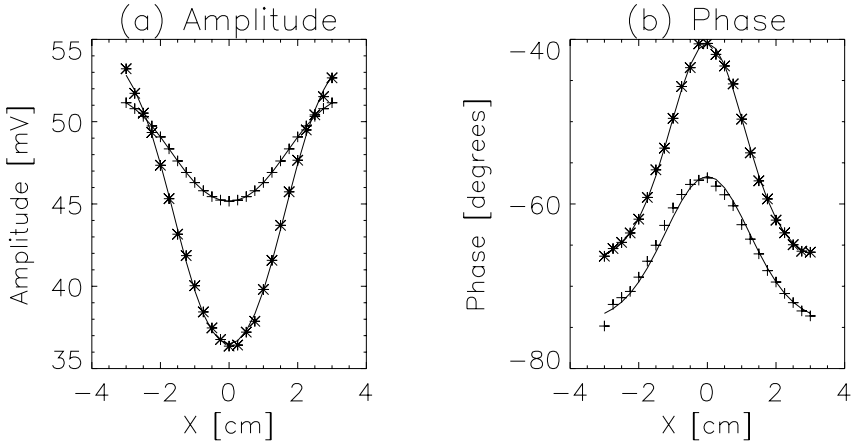

Figure 2.13: The fits to experiment C (+'s) and H (*'s) from table 2.2 for the scattering of DPDW's from purely scattering spheres. The experimental data are given by the symbols and the best fits by the solid lines. There is an arbitrary amplitude and phase difference between the two sets of data. The fits were made using the objects optical properties and initial source amplitude and phase as free parameters. The experimental parameters are given in table 2.2.

cm. With a decrease in the photon random walk step, the discrepancy between the determined radius and the known radius is seen to decrease. This trend is a result of applying the diffusion equation to a system with a sharp absorbing boundary.

To demonstrate that this least-squares fitting algorithm can be used to characterize the optical properties of spherical objects, I measured the amplitude and phase of DPDW's scattered by purely scattering objects. The objects were spheres of polystyrene resin with different concentrations of titanium-oxide (TiO_2). The method for casting these spheres is described in section 6.3. Measurements were taken along lines parallel to those indicated in fig. 2.10a with a 2.5 cm diameter object centered at x=0 and y=4 cm. The results of these experiments for spheres with different concentrations of TiO_2 are presented in table 2.2.

Fits for two of these experiments are shown in fig. 2.13. The fits agree well with the experimental data. Fits were made for spheres with eight different concentrations of TiO_2 and in all cases good agreement was found. The reduced scattering coefficient of

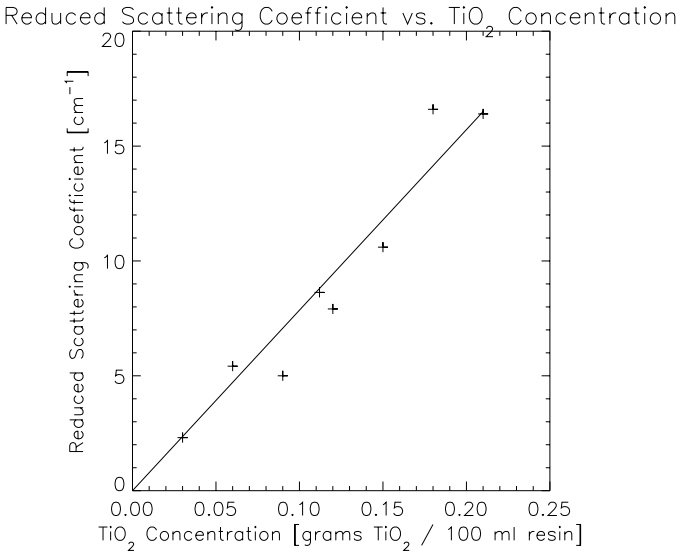

Figure 2.14: The best fits for the reduced scattering coefficients is graphed versus the TiO_2 concentration in the resin spheres. The expected linear relationship and zero intercept are observed.

the object is expected to increase linearly with the concentration of TiO_2. The data in table 2.2 show this trend. A summary of the determined reduced scattering coefficient versus TiO_2 concentration is shown in fig. 2.14. Note that the relationship is linear and that the reduced scattering coefficient goes to zero as the TiO_2 concentration goes to zero.

2.5.3 Scattering from Multiple Objects

When the sample contains two or more spherical objects, the distorted wave is calculated by summing scattering events of different order. We first calculate the scattering of the incident wave from each object. This is the first order scattered wave. The first order scattered waves are incident on and consequently scattered by the surrounding objects resulting in second order scattered waves whose amplitude is smaller than the first order wave. For two spherical objects embedded in an infinite homogeneous

Table 2.2: Results for the fitted object reduced scattering coefficient versus different TiO_2 concentrations.

	Background		TiO_2 Concentration	Object
Exp	μ_s' cm^{-1}	μ_a cm^{-1}	grams TiO_2 / 100 ml Resin	μ_s' cm^{-1}
A	2.56	0.014	0.03	2.31
B	2.56	0.014	0.06	5.42
C	2.08	0.008	0.09	5.00
D	2.08	0.008	0.11	8.63
E	1.87	0.020	0.12	7.91
F	1.91	0.018	0.15	10.6
G	2.12	0.018	0.18	16.6
H	2.15	0.015	0.21	16.4

medium, the general solution is of the form

$$\Phi_{out} = \Phi_{inc} + \sum_{n=1}^{\infty} \left(\Phi^{(n)}_{scatt,1} + \Phi^{(n)}_{scatt,2} \right) , \tag{2.44}$$

where $\Phi^{(n)}_{scatt,i}$ is the nth order scattered wave from the ith object (see fig. 2.9). While the first order waves ($\Phi^{(1)}_{scatt,i}$) are easily calculated using eq. (2.32), the second order waves ($\Phi^{(2)}_{scatt,i}$) require the solution of complex integral equations since the first order waves are not spherical. If the first order waves are spherical to a good approximation, then the second order waves can be computed analytically using the same procedure for calculating the first order scattered waves. The condition is only satisfied for small absorbing objects. In this regime we can check the significance of the second ordered scattered waves from the ratio of $\Phi^{(2)}_{scatt,i}$ to Φ_{inc}. This ratio indicates that $\Phi^{(2)}_{scatt,i}$ is negligible when

$$\left(\frac{v\delta\mu_{a,i}}{D_o} a_i^3 \right) \left(\frac{v\delta\mu_{a,j}}{D_o} a_j^3 \right) \frac{r_{sd}}{r_{si} r_{ij} r_{jd}} \exp\left(ik(r_{si} + r_{ij} + r_{jd} - r_{sd}) \right) \ll 1 , \tag{2.45}$$

where i and j denote the different objects (see fig. 2.9) and $\delta\mu_{a,i}$ is the difference in the absorption coefficient between the i^{th} object and the background.

2.5.4 Semi-Infinite Media

In medical imaging, measurements are typically made by placing the source and detector on the scalp or surface of the breast. Treating such a system as infinite is obviously incorrect and will lead to discrepancies between theory and experiment. Planar boundaries between diffusive and non-diffusive media can be modeled by requiring $\Phi_{out} = 0$ on an extrapolated zero boundary a distance $z_o = 2/(3\mu_s')$ from the actual boundary (some investigators use $z_o = 0.7104/3\mu_s'$), away from the diffusive medium [4, 76, 78, 79]. Multiple planar boundaries can be modeled by employing additional extrapolated zero boundary conditions. To first order, the extrapolated zero amplitude boundary condition is satisfied by placing an image source of negative amplitude at the position of the actual source reflected about the extrapolated

zero boundary. The photon fluence is then calculated by superimposing the DPDW's generated by the two sources and their respective scattered waves. In general, one must also consider an image of the scattered waves to ensure that Φ_{out} equals zero on the extrapolated zero boundary. These images then create waves that scatter off the object *ad infinitum*.

2.5.5 General Heterogeneous Media

In biological media the optical inhomogeneities will have arbitrary shapes. It is not possible to find analytic solutions for general heterogeneous media. We must therefore resort to numerical techniques. There are many approaches to numerically solving the diffusion equation for spatially varying optical properties, including finite difference, finite element, and perturbative methods. Here I present a short review of perturbative methods.

With a perturbative method the signal reaching the detector is considered to be a superposition of the DPDW that travelled through a homogeneous system, plus the first order scattering of DPDW's from optical inhomogeneities, plus the second order, etc. The optical properties of the background/homogeneous medium are usually taken to be the average or most common optical properties. One generally divides the region of interest (i.e. the region containing the inhomogeneity) into voxels. The first order scattered DPDW is then the scattering of the incident DPDW from each voxel. If the optical properties of the voxel are the same as the background then no wave is scattered from that voxel. The voxels are chosen to be small enough so that the scattered DPDW can be linearized, that is the amplitude of the scattered wave is linearly proportional to the change in the absorption coefficient and the change in the reduced scattering coefficient.

One way to derive the linearized scattered DPDW is to take the limiting form of Φ_{scatt} (eq. (2.33)) for small radius spheres. To leading order in $k^{out}a$ and $k^{in}a$

$$\Phi_{scatt}(\mathbf{r_s}, \mathbf{r}, \mathbf{r_d}) = v S_{AC} \frac{\exp(ik|\mathbf{r}_s - \mathbf{r}|)}{4\pi D_{out}|\mathbf{r}_s - \mathbf{r}|} \frac{\exp(ik|\mathbf{r} - \mathbf{r}_d|)}{4\pi|\mathbf{r} - \mathbf{r}_d|} \left[\frac{4\pi a^3}{3}\right]$$

$$\left\{\frac{-v\delta\mu_a(\mathbf{r})}{D_{out}}+\left[ik-\frac{1}{|\mathbf{r}_s-\mathbf{r}|}\right]\left[ik-\frac{1}{|\mathbf{r}-\mathbf{r}_d|}\right]\left[\frac{-3\delta\mu_s'(\mathbf{r})\cos\theta}{3\mu_{s,out}'+2\delta\mu_s'(\mathbf{r})}\right]\right\} \quad . \quad (2.46)$$

Here, $\delta\mu_a = \mu_{a,in} - \mu_{a,out}$ is the difference in the absorption coefficient of the voxel and background, $\delta\mu_s' = \mu_{s,in}' - \mu_{s,out}'$ is the difference in the reduced scattering coefficient, $k = k_{out}$, and θ is the angle between the line joining the source to the voxel and the line joining the detector to the voxel. The volume for a sphere of radius a appears in eq. (2.46). If the voxel is not a sphere then the $4\pi a^3/3$ must be replaced by the actual volume of the voxel.

$\Phi_{scatt}(\mathbf{r_s},\mathbf{r},\mathbf{r_d})$ is linearized by assuming that $\delta\mu_s'(\mathbf{r}) \ll \mu_s'$. The first order scattered wave reaching the detector is found by summing the contributions from each voxel. When $\Phi_{scatt}(\mathbf{r_s},\mathbf{r},\mathbf{r_d})$ is linearized then a matrix equation can be written for the first order scattered wave $\Phi_{scatt}^{(1)}$. The matrix equation is

$$\begin{pmatrix} \Phi_{scatt}^{(1)}(\mathbf{r_{s,1}},\mathbf{r_{d,1}}) \\ \Phi_{scatt}^{(1)}(\mathbf{r_{s,2}},\mathbf{r_{d,2}}) \\ \vdots \\ \Phi_{scatt}^{(1)}(\mathbf{r_{s,n}},\mathbf{r_{d,n}}) \end{pmatrix} = \begin{pmatrix} M_{1,1} & M_{1,2} & \cdots & M_{1,m} \\ M_{2,1} & M_{2,2} & \cdots & M_{2,m} \\ \vdots & \vdots & & \vdots \\ M_{n,1} & M_{n,2} & \cdots & M_{n,m} \end{pmatrix} \begin{pmatrix} \delta\mu_{a,1} \\ \delta\mu_{a,2} \\ \vdots \\ \delta\mu_{a,m} \end{pmatrix}$$

$$+ \begin{pmatrix} N_{1,1} & N_{1,2} & \cdots & N_{1,m} \\ N_{2,1} & N_{2,2} & \cdots & N_{2,m} \\ \vdots & \vdots & & \vdots \\ N_{n,1} & N_{n,2} & \cdots & N_{n,m} \end{pmatrix} \begin{pmatrix} \delta\mu_{s,1}' \\ \delta\mu_{s,2}' \\ \vdots \\ \delta\mu_{s,m}' \end{pmatrix} \quad . \quad (2.47)$$

$\Phi_{scatt}^{(1)}(\mathbf{r_{s,i}},\mathbf{r_{d,i}})$ is the first order scattered wave for the i^{th} source-detector pair, $\delta\mu_{a,j}$ and $\delta\mu_{s,j}'$ are respectively the change in the absorption and reduced scattering coefficients of voxel j relative to the background. The elements of matrix M and matrix N are given by the linearized version of eq. (2.46). Specifically,

$$M_{i,j} = vS_{AC}\frac{\exp(ik|\mathbf{r}_{s,i}-\mathbf{r}_j|)}{4\pi D_{out}|\mathbf{r}_{s,i}-\mathbf{r}_j|}\frac{\exp(ik|\mathbf{r}_j-\mathbf{r}_{d,i}|)}{4\pi|\mathbf{r}_j-\mathbf{r}_{d,i}|}\left[\frac{4\pi a^3}{3}\right]\left[\frac{-v}{D_{out}}\right] \quad , \quad (2.48)$$

and

$$N_{i,j} = vS_{AC}\frac{\exp(ik|\mathbf{r}_{s,i}-\mathbf{r}_j|)}{4\pi D_{out}|\mathbf{r}_{s,i}-\mathbf{r}_j|}\frac{\exp(ik|\mathbf{r}_j-\mathbf{r}_{d,i}|)}{4\pi|\mathbf{r}_j-\mathbf{r}_{d,i}|}\left[\frac{4\pi a^3}{3}\right] \left[ik-\frac{1}{|\mathbf{r}_{s,i}-\mathbf{r}_j|}\right]\left[ik-\frac{1}{|\mathbf{r}_j-\mathbf{r}_{d,i}|}\right]\left[\frac{\cos\theta_{i,j}}{\mu'_{s,out}}\right] , \quad (2.49)$$

where $\mathbf{r}_j$ is the position of the j^{th} voxel and $\mathbf{r}_{s,i}$ and $\mathbf{r}_{d,i}$ are the position of the i^{th} source and detector respectively.

This same matrix equation can be found directly from the heterogeneous diffusion equation. When the optical properties are spatially varying then the photon diffusion equation is

$$-\nabla D(\mathbf{r})\cdot\nabla\Phi(\mathbf{r}) - D(\mathbf{r})\nabla^2\Phi(\mathbf{r}) + v\mu_a(\mathbf{r})\Phi(\mathbf{r}) - i\omega\Phi(\mathbf{r}) = vS_0(\mathbf{r}) . \quad (2.50)$$

Separating the spatially constant terms to the left-hand side and the spatially varying terms to the right-hand side we get

$$\nabla^2\Phi(\mathbf{r}) - \frac{v\mu_{a,o}}{D_o}\Phi(\mathbf{r}) + i\frac{\omega}{D_o}\Phi(\mathbf{r}) = -\frac{v}{D(\mathbf{r})}S_0(\mathbf{r}) + \frac{1}{\mu'_{s,o}}\nabla\delta\mu'_s(\mathbf{r})\cdot\nabla\Phi(\mathbf{r}) + \frac{v\delta\mu_a(\mathbf{r})}{D_o}\Phi(\mathbf{r}) + 3\left(\mu_{a,o}-i\frac{\omega}{v}\right)\delta\mu'_s\Phi(\mathbf{r}) . \quad (2.51)$$

The solution to this equation is, after integrating $\nabla\delta\mu'_s(\mathbf{r})\cdot\nabla\Phi(\mathbf{r})$ by parts and recognizing that $\nabla^2\Phi^{(0)} = k_o^2\Phi^{(0)}$,

$$\Phi(\mathbf{r}) = \frac{vS_o\exp(ik_o|\mathbf{r}-\mathbf{r_s}|)}{4\pi D_o|\mathbf{r}-\mathbf{r_s}|} + \int\left[-\frac{v\delta\mu_a(\mathbf{r}')}{D_o}\Phi(\mathbf{r}')G(\mathbf{r}',\mathbf{r}) + \frac{\delta\mu'_s(\mathbf{r}')}{\mu'_{s,o}}\nabla\Phi(\mathbf{r}')\cdot\nabla G(\mathbf{r}',\mathbf{r})\right]d\mathbf{r}' . \quad (2.52)$$

This equation is usually solved perturbatively by assuming that $\Phi = \Phi^{(0)} + \Phi^{(1)} + \Phi^{(2)} + \cdots$. This is known as the Born approximation. Substituting this perturbative expansion into eq. (2.52) and collecting terms of like order, we obtain

$$\Phi^{(0)}(\mathbf{r_s},\mathbf{r_d}) = \frac{vS_o\exp(ik_o|\mathbf{r_d}-\mathbf{r_s}|)}{4\pi D_o|\mathbf{r_d}-\mathbf{r_s}|}$$

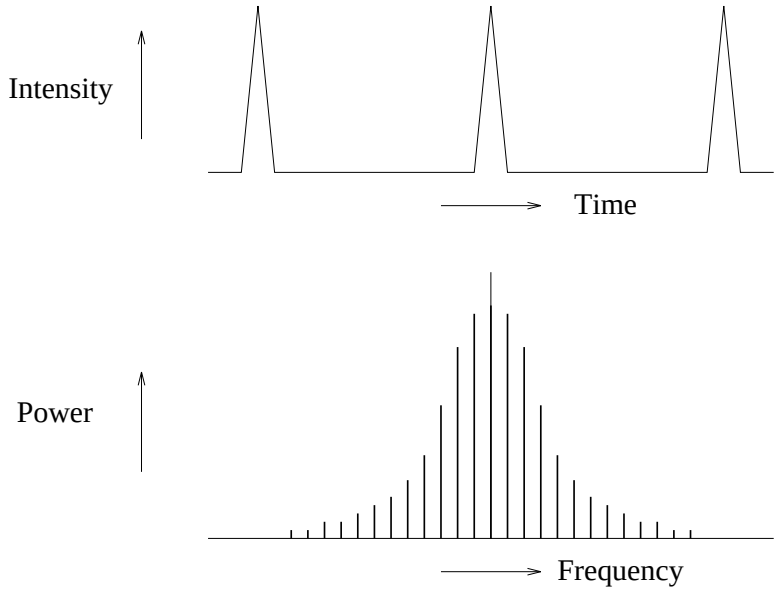

Figure 2.15: A drawing of a pulse-train from a mode-locked laser and the corresponding Fourier expansion.

$$\Phi^{(1)}(\mathbf{r_s}, \mathbf{r_d}) = \int \left[\frac{-v\delta\mu_a(\mathbf{r})}{D_o} \Phi^{(0)}(\mathbf{r_s}, \mathbf{r}) G(\mathbf{r}, \mathbf{r_d}) + \frac{\delta D(\mathbf{r})}{D_o} \nabla\Phi^{(0)}(\mathbf{r_s}, \mathbf{r}) \cdot \nabla G(\mathbf{r}, \mathbf{r_d}) \right] \mathrm{d}\mathbf{r}. \tag{2.53}$$

This equation for the first order scattered wave (first Born approximation) is identical to the equation that we obtained by summing the limiting form of the analytic solution over all voxels.

2.6 Time-Domain Measurements

The DPDW scattering theory is easily extended to the time domain. A pulse-train of light propagating in a turbid media can be thought of as a superposition of many DPDW's with different modulation frequencies (see fig. 2.15). Thus, a time resolved measurement of the propagation of a light pulse is an easy way to determine the frequency response of the system [85]. To calculate the response to a pulse of light, we simply compute the scattering due to each DPDW in parallel.

I computed the temporal evolution of a light pulse with width τ=10 ps and period T=1.0 μs in an infinite medium with different size perfect absorbers. The results indicate that the measured photon fluence decreases as a result of an absorber but that the decay rate of the fluence is relatively unaffected by its presence. These results are consistent with the experimental observations of Liu *et al.* [86].

2.7 Photon Migration within the P_3 Approximation

At optical wavelengths between 600 and 900 nm, the absorption of photons in the body is generally small compared to the corresponding scattering rate. Thus a major condition for the validity of the diffusion approximation is satisfied. The criteria is sometimes violated in hematomas, liver, and other regions with large concentrations of blood where photon absorption is large. A more accurate model of photon transport is required to describe and analyze photon migration through these systems. This section presents the P_3 solution of the transport equation [87, 88], which is a more accurate approximation for photon transport than the diffusion approximation. I demonstrate the advantages and disadvantages of the P_3 approximation for analyzing highly absorbing systems. I find that the P_3 approximation, in general, permits a more accurate determination of the reduced scattering, μ_s', and absorption, μ_a, coefficients for highly absorbing systems (i.e. $\mu_a/\mu_s' > 0.1$) or systems probed at modulation frequencies in excess of 2 to 3 GHz. In systems with highly anisotropic scattering (i.e. $\langle\cos\theta\rangle \sim 1$), determination of the reduced scattering coefficient using the P_3 approximation gives values comparable to results obtained within the diffusion (P_1) approximation.

2.7.1 P_3 Theory

The transport equation was presented in section 2.1 (eq. (2.1)) along with a description of the P_N approximation method. Here, I present the solution of the P_3 approximation and discuss the limits in which the P_3 approximation reduces to the diffusion

approximation. The P_2 equations are not solved because of inconsistencies that arise at boundaries [55].

Expanding the radiance $L(\mathbf{r},\hat{\Omega},t)$, phase function $f(\hat{\Omega},\hat{\Omega}')$, and source $S(\mathbf{r},\hat{\Omega},t)$ terms of the transport equation (eq. (2.1)) in spherical harmonics and evaluating the integral over $\mathrm{d}\hat{\Omega}'$; the transport equation is rewritten as

$$\sum_{l,m}\left[\frac{1}{v}\frac{\partial\phi_{l,m}}{\partial t}+\nabla\cdot\phi_{l,m}\hat{\Omega}+\mu_t^{(l)}\phi_{l,m}-q_{l,m}\right]Y_{l,m}(\hat{\Omega})=0\ , \tag{2.54}$$

where $\mu_t^{(l)}=\mu_s(1-g_l)+\mu_a$ (note $\mu_t^{(0)}=\mu_a$). g_l is the coefficient for the l^{th} moment of the normalized phase function. For the Henyey-Greenstein phase function, $g_l=g^l$ where g is the average cosine of the scattering angle (see appendix B). When the photon scattering is anisotropic then $\mu_t^{(l+1)}>\mu_t^{(l)}$.

Next, we multiply eq. (2.54) by $Y_{\alpha,\beta}(\hat{\Omega})$ and integrate over $\hat{\Omega}$. Using the orthogonality relations for the spherical harmonics, we obtain an infinite set of coupled linear differential equations for $\phi_{l,m}$ that agree with Kaltenbach and Kaschke [87]. See appendix A for these calculations. Within the P_3 approximation, the moments greater than $l=3$ are ignored, i.e. we set $\phi_{l,m}=0$ for $l>3$. By considering higher moments of the radiance, the P_3 approximation should be more accurate than the diffusion approximation. However, the P_3 approximation will break down as the anisotropy of the radiance is increased by increasing photon absorption and/or the DPDW modulation frequency.

Working in the frequency domain (i.e. $\partial/\partial t\rightarrow -i\omega$), the equation for $\phi_{0,0}$ in a homogeneous medium is

$$\left[9\nabla^4+\beta\nabla^2+\gamma\right]\phi_{0,0}(\mathbf{r},\omega)=Wq_{0,0}(\mathbf{r},\omega)+Xq_{1,0}(\mathbf{r},\omega)+Yq_{2,0}(\mathbf{r},\omega)+Zq_{3,0}(\mathbf{r},\omega)\ , \tag{2.55}$$

where

$$\beta=90\frac{\omega^2}{v^2}+i\frac{\omega}{v}\left(55\mu_a+27\mu_t^{(1)}+35\mu_t^{(2)}+63\mu_t^{(3)}\right)-\left(27\mu_a\mu_t^{(1)}+28\mu_a\mu_t^{(3)}+35\mu_t^{(2)}\mu_t^{(3)}\right) \tag{2.56}$$

$$\gamma=105(-i\frac{\omega}{v}+\mu_a)(-i\frac{\omega}{v}+\mu_t^{(1)})(-i\frac{\omega}{v}+\mu_t^{(2)})(-i\frac{\omega}{v}+\mu_t^{(3)})\ , \tag{2.57}$$

and the right-hand-side of eq. (2.55) contains the moments of the source distribution. The coefficients W, X, Y, and Z are given in section A.1.2 by eq. (A.34), eq. (A.35), eq. (A.36), and eq. (A.37) respectively.

Let's assume that the source is an isotropic point source such that $q_{l,0} = 0$ for $l > 0$. For an infinite medium, the solution of eq. (2.55) is of the form

$$\phi_{0,0} \propto \frac{1}{4\pi r} \exp(ik_{p3}r) \ , \tag{2.58}$$

where k_{p3} is given by

$$k_{p3}^2 = \frac{\beta \pm \sqrt{\beta^2 - 36\gamma}}{18} \ . \tag{2.59}$$

Here I concentrate on the negative root. The positive root contributes to the solution only within a few mean free paths of the source. This solution has been discussed previously [88], particularly with regards to the positive root and the appropriate boundary conditions for semi-infinite media.

For typical parameters where the diffusion approximation is known to be valid, $|36\gamma/\beta^2| \ll 1$. For example, using $\mu_s = 100.0$ cm^{-1}, $\mu_a = 0.1$ cm^{-1}, $g = 0.9$, and $\omega = 0$, we see that $36\gamma/\beta^2 = 0.005$. Eq. (2.59) can then be expanded to first order, giving

$$k_{p3}^2 = \frac{\beta}{18}\left(1 - \sqrt{1 - \frac{36\gamma}{\beta^2}}\right) \approx \frac{\gamma}{\beta} \approx 3\mu_t^{(1)}(-\mu_a + i\frac{\omega}{v}) = k_{diff}^2 \ . \tag{2.60}$$

This is the well known wavenumber solution from the diffusion equation (see eq. (2.14) [21]). In the regime where the diffusion approximation is known to be valid, eq. (2.56) and eq. (2.57) can be approximated as

$$\beta = -35\mu_t^{(2)}\mu_t^{(3)} \tag{2.61}$$

$$\gamma = 105(-i\frac{\omega}{v} + \mu_a)\mu_t^{(1)}\mu_t^{(2)}\mu_t^{(3)} \ . \tag{2.62}$$

Thus, for these parameters, the P_3 solution reduces to the diffusion solution, indicating that the diffusion equation is valid when $|36\gamma/\beta^2| \ll 1$, i.e.

$$|\frac{108}{35}(\mu_a - i\frac{\omega}{v})\frac{\mu_t^{(1)}}{\mu_t^{(2)}\mu_t^{(3)}}| \ll 1 \ . \tag{2.63}$$

For systems that do not satisfy this condition, it is believed that the full solution of the P_3 equation would more accurately approximate photon transport through the system. Furthermore, from this condition, we see that the limits of validity of the diffusion equation can be checked by: (1) increasing μ_a relative to μ_s, (2) increasing ω/v relative to μ_s, and (3) decreasing the scattering anisotropy factor while holding μ_s' constant.

2.7.2 Comparison of P_3 and Diffusion Theories

To test the usefulness of the P_3 approximation compared to the diffusion approximation, I first generated data for known parameters using a Monte Carlo computer code for photon transport in an infinite, homogeneous system. The code is explained in section 6.1.2 and supplied in appendix C. The Monte Carlo code was used to find the temporal response to a pulse of light injected into a homogeneous, infinite medium for various optical properties and scattering anisotropies. I then used the generated data to compare diffusion theory and P_3 as a function of μ_a, the modulation frequency ω (by Fourier transforming the data) and the scattering anisotropy. The comparison was made by fitting amplitude and phase data versus the source-detector separation using the P_3 solution and diffusion solution to find μ_s' and μ_a. Source-detector separations ranging from 2.0 to 4.0 cm, in steps of 0.2 cm, were used.

Fig. 2.16 displays the optical properties determined from the Monte Carlo data using the P_3 approximation and the diffusion approximation versus the known absorption coefficient of the medium. Results are plotted for data generated with two different anisotropy factors. All results in fig. 2.16 are for a modulation frequency of 390 MHz. The analysis based on the P_3 approximation is significantly better than diffusion theory at determining the correct μ_s' when the scattering is isotropic, i.e. $g = 0$, and the absorption coefficient exceeds 10% of the known reduced scattering coefficient. A similiar difference is observed for the determined absorption coefficient. For anisotropic scattering ($g = 0.9$), we see that in finding μ_s' the P_3 approximation is not as good as the diffusion approximation when $\mu_a/\mu_s' < 0.2$, although P_3 still en-

ables a more accurate determination of μ_a. This is most likely a result of a premature truncation of the spherical harmonic expansion of the phase function in arriving at the P_3 theory. In diffusion theory the anisotropy is implicitly contained in the reduced scattering coefficient, while in the P_3 theory the anisotropy is expressed explicitly. Modifying the P_3 theory with the δ-E(4) approximation discussed by Star [88] may improve the determination of μ_s'. Basically, within the δ-E(4) approximation, a delta function is added to spherical harmonics expansion of the phase function (eq. (2.6)) to compensate for the truncation.

To investigate the accuracy of the diffusion approximation and the P_3 approximation for high modulation frequencies, I used Monte Carlo data for a system with $\mu_s' = 10.0$ cm^{-1} and $\mu_a = 0.50$ cm^{-1} and calculated the optical properties using both approximations for frequency components ranging from 0 to 6 GHz. The results are plotted in fig. 2.17 for a system with isotropic scattering (fig. 2.17 a and b) and anisotropic scattering with $g = 0.9$ (fig. 2.17 c and d). In the case of isotropic scattering, the P_3 approximation is in general more accurate than diffusion theory, although diffusion theory is accurate to 5% for modulation frequencies less than 4 GHz. For anisotropic scattering, however, μ_s' is more accurately determined by diffusion theory up to 6 GHz, while P_3 is superior for determining μ_a. Similar trends are observed for different absorption coefficients.

2.8 Summary

We have seen that the migration of photons in highly scattering media can be treated by the photon diffusion equation. For an intensity modulated source, the diffusion equation predicts a coherent photon density waves that propagate spherically outwards from the source, and this has been observed. Although microscopically the photons are individually following a random walk, macroscopically they produce a coherent intensity wave. The properties of this intensity wave can be understood using conventional optics. This was demonstrated experimentally with the refraction of DPDW's

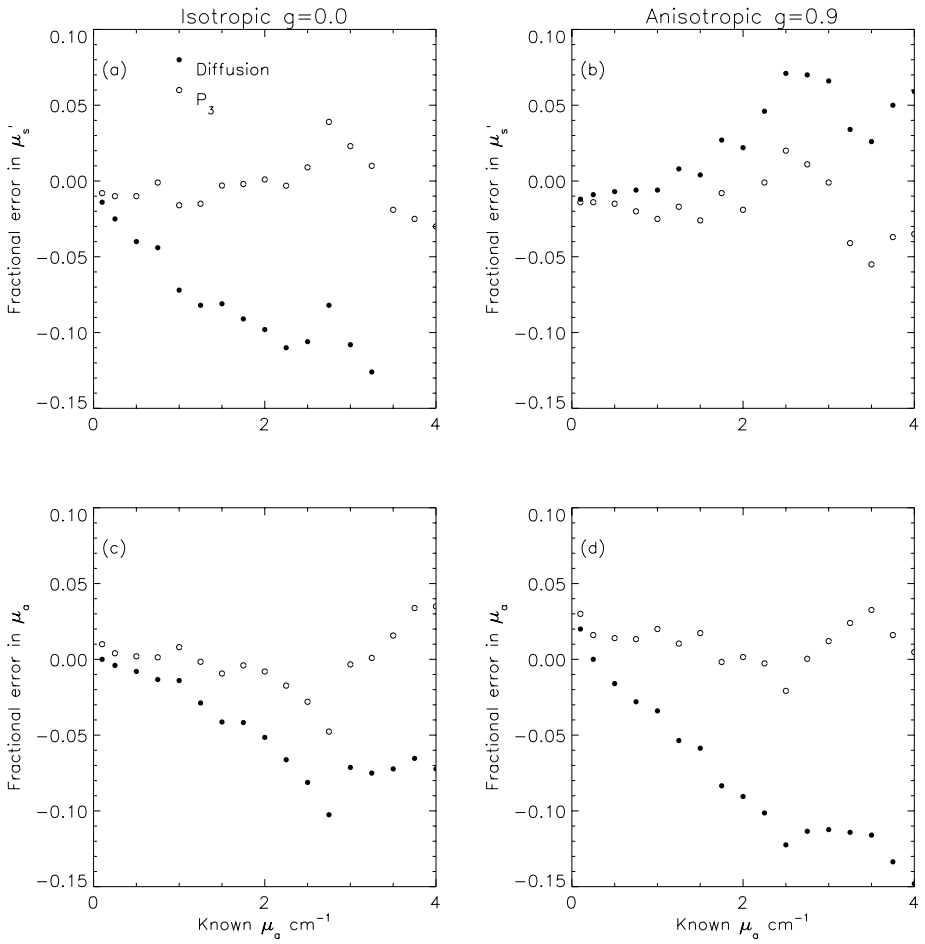

Figure 2.16: A comparison of diffusion theory (closed circles) and the P_3 approximation (open circles) for finding the scattering (top) and absorption (bottom) properties of an infinite system is presented as a function of the known absorption coefficient of the medium (μ_s' was fixed at 10.0 cm^{-1}). The results for isotropic scattering are presented in (a) and (b), and the anisotropic results are given in (c) and (d).

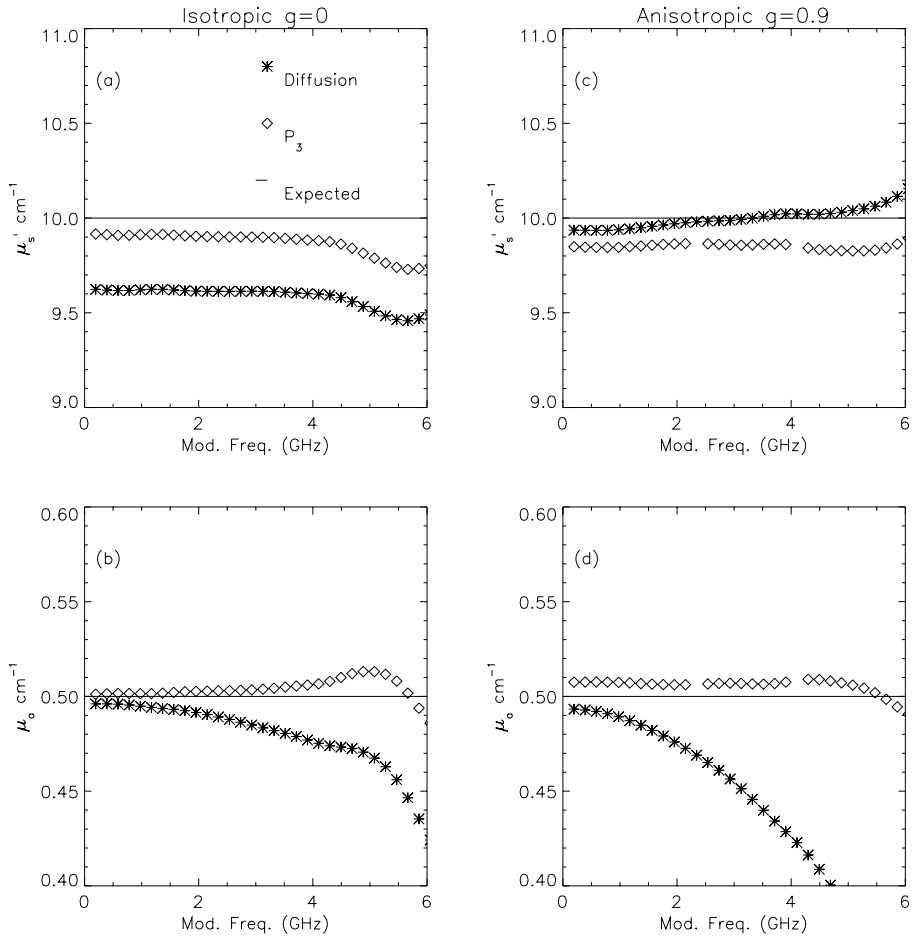

Figure 2.17: Optical properties determined using diffusion theory (stars) and P_3 (diamonds) are compared with the known optical properties (solid line) as a function of the modulation frequency. The results for isotropic scattering are presented in (a) and (b), and the anisotropic results are given in (c) and (d).

at a planar interface between two different scattering media, and the refraction, diffraction, and scattering by spherical inhomogeneities. Interestingly, the scattering is accurately modeled by an analytic solution of the Helmholtz equation and is analogous to a scalar version of Mie Theory for the scattering of electromagnetic waves from dielectric spheres. Experimental observations demonstrate that this solution can be used in conjunction with a simple imaging algorithm to characterize spherical objects. Finally we looked at higher order approximations to the transport equation, specifically the P_3 approximation, and found that the applicability of DPDW's could be extended to probe highly absorbing media such as liver and hematomas.